

Crystallographic, optical and electronic properties of the $\text{Cs}_2\text{AgBi}_{1-x}\text{In}_x\text{Br}_6$ double perovskite: understanding the fundamental photovoltaic efficiency challenges

Laura Schade¹, Suhas Mahesh¹, George Volonakis², Marios Zacharias³, Bernard Wenger¹, Felix Schmidt⁴, Sameer Vajjala Kesava¹, Dharmalingam Prabhakaran¹, Mojtaba Abdi-Jalebi⁵⁻⁶, Markus Lenz⁴, Feliciano Giustino⁷⁻⁸, Giulia Longo⁹, Paolo G. Radaelli¹ and Henry J. Snaith¹

¹ Clarendon Laboratory, Department of Physics, University of Oxford, Oxford OX1 3 PU, United Kingdom

² Univ Rennes, ENSCR, INSA Rennes, CNRS, ISCR (Institut des Sciences Chimiques de Rennes), UMR 6226, France

³ Department of Mechanical and Materials Science Engineering, Cyprus University of Technology, P.O. Box 50329, 3603 Limassol, Cyprus

⁴ University of Applied Sciences and Arts Northwestern Switzerland (FHNW), School of Life Sciences, Institute for Ecopreneurship, 4132 Muttenz, Switzerland

⁵ Institute for Materials Discovery, University College London, Torrington Place, London, WC1E 7JE, United Kingdom

⁶ Cavendish Laboratory, Department of Physics, University of Cambridge, JJ Thomson Avenue, Cambridge CB3 0HE, United Kingdom

⁷ Oden Institute for Computational Engineering and Sciences, The University of Texas at Austin, Austin, Texas 78712, USA

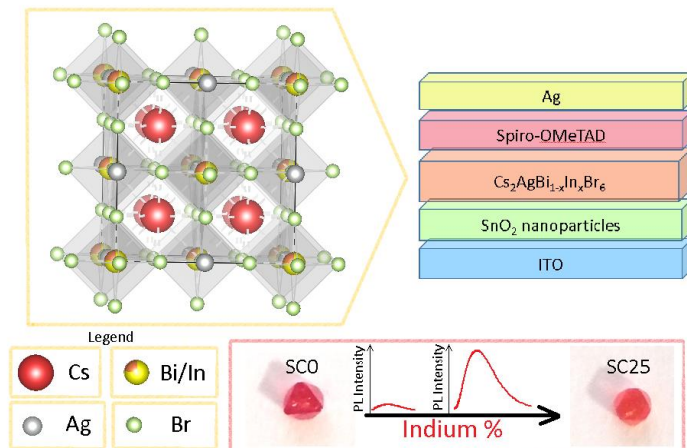
⁸ Department of Physics, The University of Texas at Austin, Austin, Texas 78712, USA

⁹ Department of Mathematics, Physics and Electrical Engineering, Northumbria University, Ellison place, Newcastle upon Tyne NE18ST, United Kingdom

Abstract

We present a crystallographic and optoelectronic study of the double perovskite $\text{Cs}_2\text{AgBi}_{1-x}\text{In}_x\text{Br}_6$. From structural characterization we determine that the indium cation shrinks the lattice and shifts the cubic-to-tetragonal phase transition point to lower temperatures. The absorption onset is shifted to shorter wavelengths upon increasing the indium content, leading to wider band-gaps, which we rationalize through first-principle band structure calculations. Despite the unfavorable band gap shift, we observe an enhancement in the steady-state photoluminescence intensity, and *n-i-p* photovoltaic devices present higher short circuit current than neat $\text{Cs}_2\text{AgBiBr}_6$ devices. In order to evaluate the prospects of this material as a solar absorber, we combine accurate absorption measurements with thermodynamic modeling and identify the fundamental limitations of this system. Provided radiative efficiency can be increased, and the selection of charge extraction layers specifically improved, this material could prove to be a useful wide band-gap solar absorber.

TOC GRAPHICS



The power conversion efficiency of photovoltaic devices based on hybrid halide perovskite materials has increased to a remarkable 25.2% in the past few years [1-4], and light emitting diodes (LEDs) based on metal halide perovskites already match with organic LEDs, in terms of electroluminescence external quantum efficiency [5]. The highest efficiency devices are based on organic-inorganic lead halide perovskites [6-9], however, there are some non-ideal aspects related to these materials which could be circumvented with the discovery of new compounds. In particular, the presence of an organic cation in the crystal implies relatively low thermal stability, which may hinder the successful introduction of the devices to some commercial markets [10-13]. Furthermore, for optoelectronic applications beyond photovoltaics, the presence of lead may prove challenging since electronic devices need to comply with the restriction of hazardous substances (RoHS), which limits the admissible quantity of lead in a solid layer.

Inorganic perovskites based on non-toxic metals are attractive alternatives to lead-halide perovskites, and have driven the research community towards the study of inorganic metal halide semiconductors with improved functionality [14-16]. Over the last few years, double perovskite

materials have emerged as possible contenders [17]. In particular the double perovskite $\text{Cs}_2\text{AgBiBr}_6$ has been the subject of several studies that have revealed excellent environmental stability and promising optoelectronic properties [18-21]. Nevertheless, the efficiency obtained so far for this material employed as the absorber layer in solar cells is still very low (2.2%) [22], and it is unclear if it will be able to match the optoelectronic properties of lead halide perovskites.

The optical properties and the stability of perovskite materials can be significantly influenced by external conditions, such as applying high temperature or pressure, but also via chemical alloying [23]. With this approach, Du et al. [24] engineered the bandgap of the $\text{Cs}_2\text{AgBiBr}_6$ double perovskite using trivalent metal alloying with In^{III} and Sb^{III} , finding that the first enhances the photoluminescence (PL) intensity, while the second one induces a substantial decrease of the PL emission. Furthermore, Luo et al. [25] have demonstrated extremely high photoluminescence quantum yield and electroluminescence efficiency for $\text{Cs}_2\text{AgInCl}_6$ when substituting Ag^{I} for Na^{I} and doping with small concentrations of Bi.

Here, we explore the influence of In^{III} alloying on the structural optical and electronic properties of the $\text{Cs}_2\text{AgBiBr}_6$ double perovskite. We synthesized excellent-quality single crystals with compositions of up to ~25% indium at the B' site, and polycrystalline powders with up to ~80% of indium content ($\text{Cs}_2\text{AgBi}_{0.2}\text{In}_{0.8}\text{Br}_6$). In addition, we prepared high-quality double-perovskite thin-films with a range of indium content. Using variable-temperature single crystal/powder X-ray diffraction (XRD) and heat capacity measurements, we discover that the low-temperature cubic-to-tetragonal phase transition, previously reported for the neat compound [26], shifts to lower temperatures as indium is added to the structure. We determine the amount of indium present through XRD structural characterization, and further confirm the values with inductively

coupled plasma mass spectrometry (ICP-MS). Beyond crystallographic characterization, we investigate the optoelectronic behavior of the neat and alloyed $\text{Cs}_2\text{AgBiBr}_6$ materials, and we find that a relatively small amount of indium on the B site enhances the photoluminescence intensity and shifts the bandgap to higher energies. Using density functional theory (DFT), we investigate the influence of indium on the electronic band structure. Moreover, we prepared *n-i-p* solar cell devices with and without indium in the double perovskite layer, and highlight the improvements in the performance: the open-circuit voltage of devices with indium is higher than the ones without it, delivering a higher power conversion efficiency (PCE). Further calculations show that the device open-circuit voltage can be severely affected by the shallow optical absorption edge whose Urbach energy exceeds $k_B T$ (where k_B is the Boltzmann constant and $T=300\text{K}$).

For clarity, in our figures we will present the data measured on single crystals in red, on polycrystalline powders in green, and on thin films in blue. For the synthesis of $\text{Cs}_2\text{AgBi}_{1-x}\text{In}_x\text{Br}_6$ single crystals, we followed a modified version of the synthesis route previously reported for $\text{Cs}_2\text{AgBiBr}_6$ double perovskite [26]. We dissolved the precursors (CsBr, AgBr, BiBr₃) in DMSO and precipitated with acetone to form a polycrystalline powder. We then dissolved the as-synthesized powder in hot HBr (at about 100°C) and added InBr₃ to this hot solution in different proportions. Cooling down to room temperature at a rate of half a degree per hour, we managed to grow single crystals with a range of indium contents. With this method we prepared 5 different alloyed crystals in addition to the neat Bi double perovskite (SC0): SC1, SC7, SC12, SC17 and SC25 with $\approx 1\%$, 7%, 12%, 17% and 25% of indium respectively. The percentages indicate the amount of indium on the bismuth site, and refer to the compositions of the as-synthesized crystals, which we deduced from ICP-MS (see table ST1 in the Supplementary information (SI)). The

results of the XRD-fittings on single crystals are shown in Figure S1 in the SI, and they demonstrate excellent crystal quality. Results of the fittings are reported in Table ST2. Single crystals grown through this solution-process method allowed us to achieve a maximum of 25% of indium to be substituted on the bismuth site. In addition, through a solid-state synthesis method [24] we prepared 5 polycrystalline samples with different indium concentrations all the way up to 60% indium substitution, once again confirmed by ICP-MS (values in table ST4). For simplicity, we will denote the powder samples according to their indium content, as PW0, PW10, PW35, PW45, PW60 and PW80. The polycrystalline powders XRD patterns with their Rietveld refinement and the crystallographic results are shown in Figure S2 and table ST3 in the Supplementary Information. We also prepared thin films of the $\text{Cs}_2\text{AgBi}_{1-x}\text{In}_x\text{Br}_6$ double perovskite by spin-coating a solution of the dissolved polycrystalline powders in DMSO (dimethyl-sulfoxide) on quartz or glass, and then heating for 5 minutes on a hot plate at about 285°C in ambient atmosphere. The heating time was adapted slightly depending on the alloying, to prevent crystallization of impurity phases in the film. Similar to the previous nomenclature, we will denote the thin films TF0, TF10, TF35, TF45, TF60, and TF80 in relation to the percentage of indium evaluated through the ICP-MS measurement of the precursor powders. The thickness of the different thin films is reported in Table ST5 and the XRD-patterns are shown in Figure S3.

The XRD analysis reveals that all the samples are cubic at room temperature, consistent with space group $\text{Fm}\bar{3}\text{m}$, the same as the neat $\text{Cs}_2\text{AgBiBr}_6$ compound. Moreover, the lattice contracts as the indium cation replaces the smaller bismuth, translating into a peak shift of all reflections towards higher angles. This is demonstrated in Figure 1a and 1b, zooming into the (400) peak. The slight mismatch between the peak positions of the thin films and of the polycrystalline powders is due to experimental uncertainties in the powder diffractometer (e.g. the refined zero point and the height

of the sample in the holder), while the peak positions in the patterns of the thin films samples have been calibrated to the known peak positions of the quartz substrate. This discrepancy doesn't affect our conclusion since its effect on the lattice parameters is much smaller than the shift in peak positions due to changes in composition.

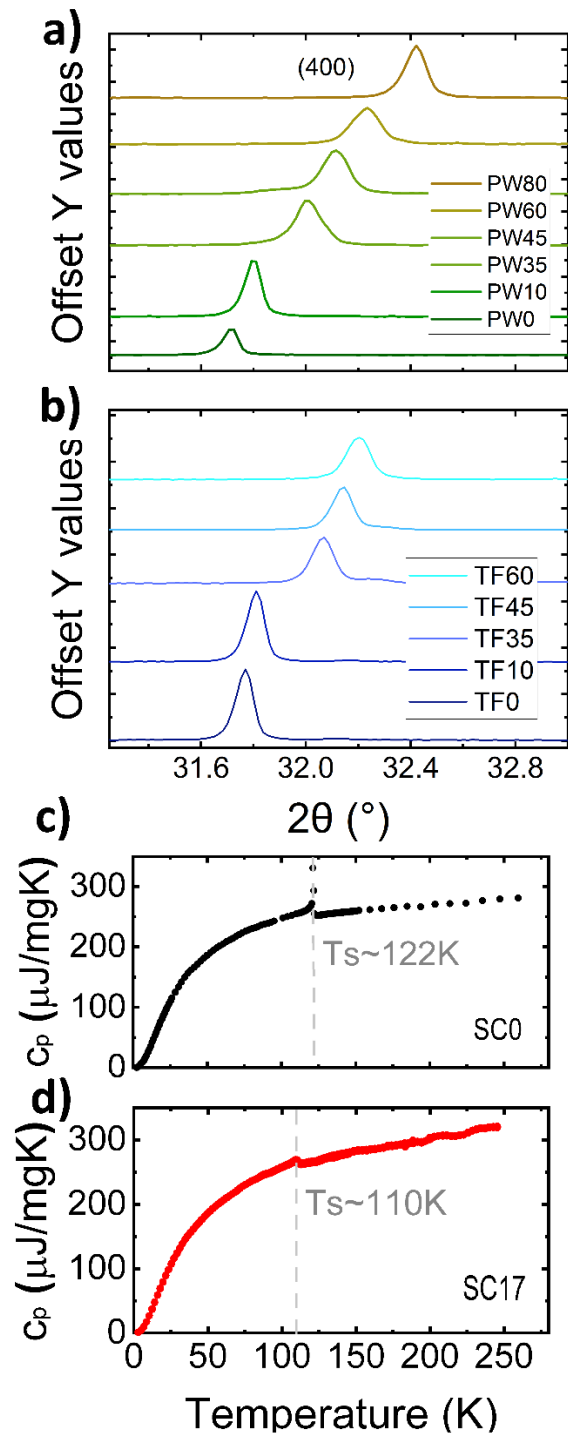


Figure 1 XRD patterns in the region of the (400) peak for a) polycrystalline powders and b) thin films of the $\text{Cs}_2\text{AgBi}_{1-x}\text{In}_x\text{Br}_6$ double perovskite samples and specific heat capacity measured on single crystals c) SC0 and d) SC17.

To further investigate the impact of alloying indium in the $\text{Cs}_2\text{AgBiBr}_6$ double perovskite, we performed temperature-dependent heat capacity and low-temperature X-ray diffraction measurements. For $\text{Cs}_2\text{AgBiBr}_6$ a cubic-to-tetragonal phase transition occurs at $\sim 122\text{K}$ [26], as shown in Figure 1c. With the substitution of bismuth with indium, this phase transition temperature monotonically shifts to lower temperature, for instance being at $\sim 110\text{K}$, for SC17 as we show in Figure 1d (see Section 2 of the SI for details). It also appears that the specific heat anomaly at the transition temperature becomes smoother with increasing indium content, and disappears altogether in the case of SC25, as shown in Figure S6c in the SI. However, the temperature-dependent X-ray diffraction measurements (see SI) clearly indicate that the transition is still present in the PW35 composition, only shifting to a lower temperature of 60K (Figure S5). The disappearance of the heat capacity singularity at the transition point for higher concentrations of indium can be explained if we classify the transition of the $\text{Cs}_2\text{AgBiBr}_6$ neat perovskite to be close to a tricritical point, i.e., to the crossover between a first- and a second-order transition. At first proposed by B. Wruck in 1986 for the $\text{I}\bar{1}$ - $\text{P}\bar{1}$ transition in anorthite [27], disorder can change both the transition temperature and the order of the transition. This leads to the rapid disappearance of the lambda-anomaly in the heat capacity in anorthite samples that have been either heat-treated or contaminated with Na, which instead display a smeared-out stepwise increase of excess heat capacity. This happens because the transition, being initially close to a tricritical point, moves deeper into the second-order regime when Na is added, leading to a crossover from a lambda-singularity to a step-singularity. We observe an analogous behavior for our samples, with the difference that in our measurements with high concentration of indium,

the smeared-out step appears to be too small to be detected, particularly since it occurs in a rapidly changing region of the heat capacity curve.

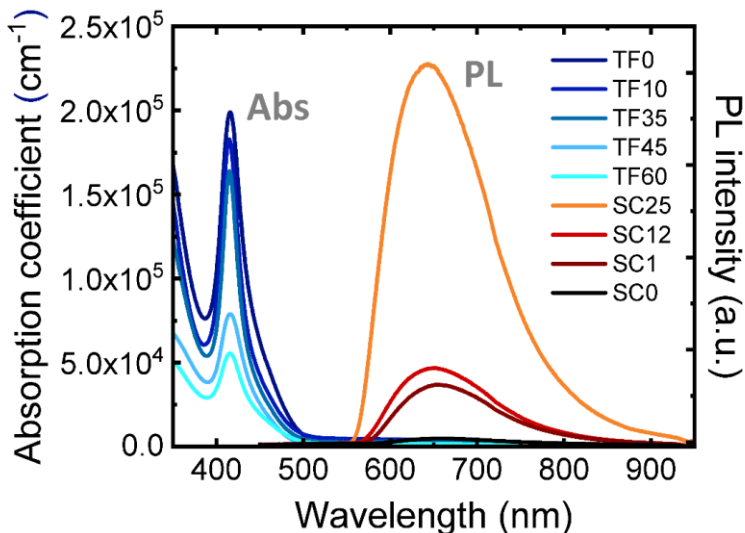


Figure 2 Absorption coefficient measured on $\text{Cs}_2\text{AgBi}_{1-x}\text{In}_x\text{Br}_6$ thin films from UV-vis measurements and steady-state photoluminescence of $\text{Cs}_2\text{AgBi}_{1-x}\text{In}_x\text{Br}_6$ single crystals.

To explore the influence of indium on the opto-electronic properties of the double perovskite material, we performed steady-state photoluminescence spectroscopy on both single crystals and polycrystalline powders. We note that we could not detect a strong PL signal from the thin films, and hence measured the PL directly from the surface of the solid-samples, employing a fiber-coupled laser for excitation, with detection directly through a fiber-boudele in close proximity to the excitation (see SI for further details). Figure 2 shows the emission from single crystals with different indium contents. The addition of indium clearly enhances the photoluminescence, with the PL intensity of SC25 being about 100 times higher in comparison to the neat Bi crystal. In Figure S7a of the SI, we show the photoluminescence emission from polycrystalline powders of $\text{Cs}_2\text{AgBi}_{1-x}\text{In}_x\text{Br}_6$. Notably, these were detectable, but lower of intensity than the single crystals,

presumably due to smaller crystallite size, increased surface area, and increased surface defect density. The trend up to PW35 agrees with an increase in emission intensity and is consistent with the measurements on single crystals, while the PL starts decreases gradually for higher indium content. In both single crystals and powders, it is noticeable that the PL peak maximum also shifts slightly towards higher energies when indium is added to the structure, as shown in Figure S7b in the SI, consistent with a lattice contraction leading to a widening of the band gap.

The absorption coefficient, measured with UV-Vis absorption spectroscopy on thin films, is also shown in Figure 2. We notice a pronounced resonant absorption feature centered at $\sim 420\text{nm}$, as previously reported in literature [21,28]. There is still debate about the origin of this feature, which has been associated with trapped excitonic transitions below the high energy direct bandgap [21,28-30] or to intra-band transitions [31,32]. The overall absorption strength decreases with increasing indium content. This decrease is further confirmed by the extinction coefficient obtained from spectroscopic ellipsometry measurements of the single crystals (shown in Figure S9 of the SI). The alloyed double perovskite maintains the same main features of neat $\text{Cs}_2\text{AgBiBr}_6$ in absorption and emission, with a decrease in absorption and an increase in photoluminescence emission intensity for low indium content ($<35\%$). The increased PL intensity indicates fewer, or less active, defect sites responsible for trap-assisted recombination, suggesting that the introduction of a small amount of indium may enhance the electronic properties of $\text{Cs}_2\text{AgBi}_{1-x}\text{In}_x\text{Br}_6$ for use as photoactive layers in devices.

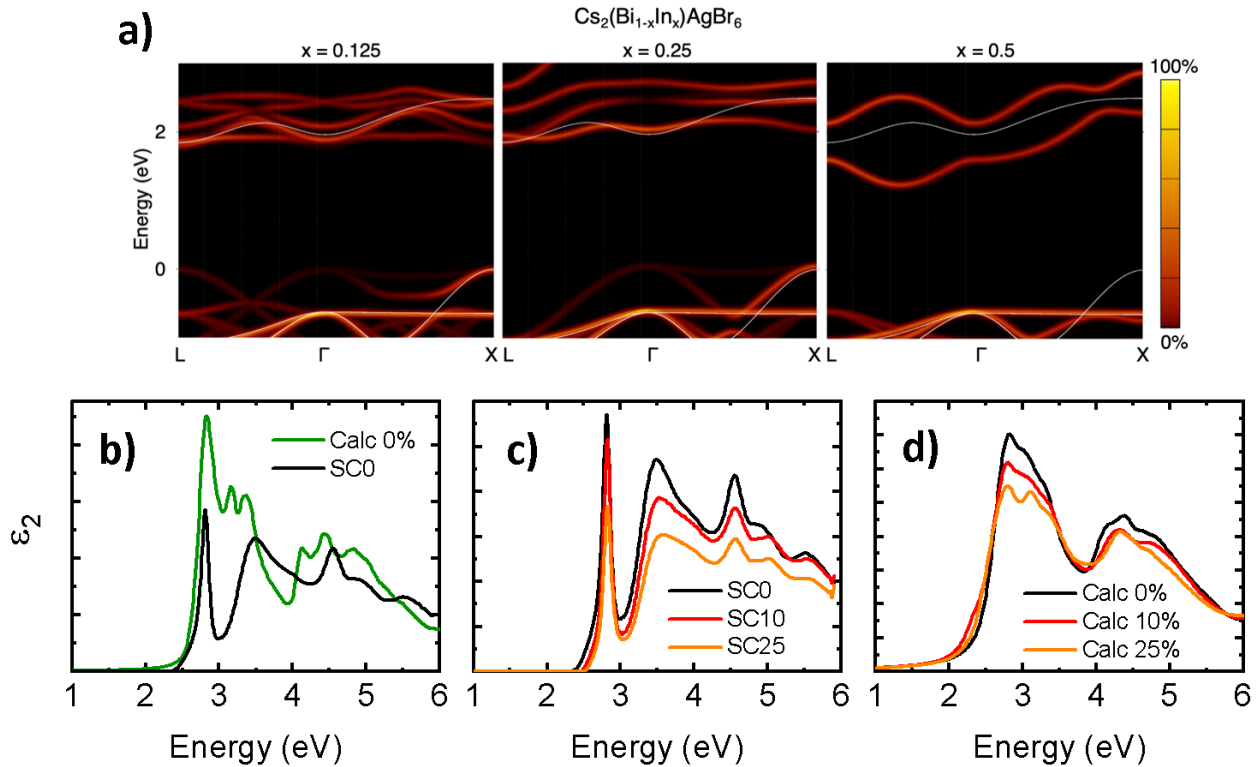


Figure 3 a) Calculated spectral functions for the $\text{Cs}_2\text{AgBi}_{1-x}\text{In}_x\text{Br}_6$ double perovskite for $x=0.125$, 0.25 and 0.5 , using the unfolding procedure described in text (the color map represents the spectral weight/occupation probability of each state). For comparison, the band dispersion of neat of $\text{Cs}_2\text{BiAgBr}_6$ is shown as a white line. b) Calculated (green) and measured (black) imaginary part of the dielectric function of $\text{Cs}_2\text{BiAgBr}_6$. c) Experimental and d) calculated imaginary part of the dielectric function as a function of indium content. Experimental values were extracted from ellipsometry data on single crystals SC0, SC10 and SC25.

To further understand the changes in the optical properties when indium is introduced to the structure, we calculated the electronic band structures of $\text{Cs}_2\text{AgBi}_{1-x}\text{In}_x\text{Br}_6$ by employing density functional theory (DFT), using a $2 \times 2 \times 2$ supercell of the $\text{Fm}\bar{3}m$ double perovskite (details in the SI). For the different indium concentrations (i.e. $x=0.125$, 0.25 , 0.5) we replaced 1, 2, and 4 bismuth atoms with indium, respectively, as shown in Figure S10 of the SI. We chose to maximize

the distance between neighboring indium atoms and place these in the most uniform way in the supercell. The lattice parameters were kept fixed at the measured values while we performed only an optimization of the atomic positions within DFT-PBE (details in the SI). To obtain the band structure and compare them with the band structure of pristine $\text{Cs}_2\text{AgBiBr}_6$, we calculated the supercell states of the doped systems and map them onto the Brillouin zone of neat $\text{Cs}_2\text{AgBiBr}_6$ (see computational methods in the SI) [33,34]. The spectral functions of the indium-doped $\text{Cs}_2\text{AgBiBr}_6$ are shown in Figure 3a as a color map representing the momentum-resolved electronic density of states. The resulting spectral functions are calculated along the L- Γ -X path of the larger Brillouin zone and are shown in Figure 3a, with the white lines showing the band structure of $\text{Cs}_2\text{BiAgBr}_6$. For the electronic structure we used the difference $E_{G_HSE}-E_{G_DFT}$ at the Γ point to rigidly shift the conduction bands calculated within DFT-PBE. There are two main features appearing upon introducing indium into the material. First, the appearance of a new band within the conduction band manifold, which is related to indium s-orbitals. As indium concentration increases, this band moves to lower energies and becomes more dispersive. This is consistent with the band structure of pristine $\text{Cs}_2\text{AgInX}_6$ ($x = \text{Cl}, \text{Br}$) for which the conduction band bottom consists of a dispersive band associated with indium s-orbitals [35]. Secondly, the valence band top of $\text{Cs}_2\text{BiAgBr}_6$ at X slowly disappears. In fact, when the Bi-Ag network is completely disrupted along all directions (50% model) the valence band top is shifted to the Γ position, similar to the valence band exhibited in neat $\text{Cs}_2\text{InAgX}_6$ ($X=\text{Cl}, \text{Br}$) compounds. Interestingly, for indium-alloying of up to 25% the band edges (i.e. the valence band top, and conduction band bottom) show minimal changes, while upon reaching 50% indium concentration the band extrema character resemble more the case of pristine $\text{Cs}_2\text{InAgBr}_6$ [35], due to the lower energy of indium s-orbitals and the dominance of Ag d-orbitals at the valence band top. As we can see in Figure 3, the band

gap of all the materials is indirect and the gap is slightly decreasing upon increasing indium concentration. The calculated band gap decrease is consistent with calculations on the pristine $\text{Cs}_2\text{AgBiBr}_6$ and $\text{Cs}_2\text{AgInBr}_6$, for which the calculated band gaps are of 1.97 (2.60) eV and 1.44 (2.09) eV, respectively, within HSE (PBE0) hybrid functional. Yet, this band gap trend is in contrast with our experimental observations, where in Figure 2 we saw that the absorption onset (and the PL maxima) shifts to shorter wavelength upon indium alloying. Consequently, higher level calculations are required to accurately predict the band gaps of both the compounds and their alloys. For consistency, here we choose to employ the HSE hybrid functional including spin-orbit coupling on the supercells, which is known to accurately predict the gap of pristine $\text{Cs}_2\text{AgBiBr}_6$, which is the starting point of our work.

We further explored the optical effects for the In-alloyed double perovskite through first-principles calculations of the dielectric function. Figure 3b shows the calculated (green) and measured (black) imaginary part of the dielectric function for pristine $\text{Cs}_2\text{AgBiBr}_6$, where the latter one has been obtained from the n and k coefficients of Figure S9 following the formula: $\varepsilon_2=2nk$. Overall, the position of the main features measured for $\text{Cs}_2\text{AgBiBr}_6$ are described relatively well by our independent-particle calculations. We can even tentatively assign the intense peak in the absorption at 2.8 eV to inter-band transitions related to the presence of the separated electronic band at the bottom of the conduction band of $\text{Cs}_2\text{AgBiBr}_6$. The exact shape and separation of the absorption peaks close to the onset would require calculations that include electron-hole interactions to probe the strength of electron-hole renormalization effects and the presence of excitonic enhancement effects near the band edge. Figure 3d shows the calculated imaginary part of the dielectric function of $\text{Cs}_2\text{AgBi}_{1-x}\text{In}_x\text{Br}_6$ double perovskite for different indium contents. These calculations involve the large super-cells used for the electronic structure calculations, with

optimized atomic positions and using the experimental lattice parameters measured by XRD. For consistency, the dielectric function of pristine $\text{Cs}_2\text{AgBiBr}_6$ shown in panel d is calculated using a large $2\times 2\times 2$ super-cell, hence we note the slight difference in the applied smearing between panels b and d, as detailed in the SI. We can notice that the overall intensity decreases with increasing indium content, consistent with the experimental data shown in panel c. In summary, based on our theoretical analysis of the optical changes occurring with indium alloying, we can consistently explain the origin of the reduced absorption intensity, which we assign to the increasing contribution of indium s-orbitals and the reduced contribution of bismuth s-orbitals, to the valence band minima and other concurrent changes in the band structure. However, the small shift in overall band gap which we determine theoretically, occurs in the opposite direction to what we have determined experimentally. This suggests that a more realistic modelling of indium incorporation using larger supercells, as well as an improved description of the optical properties beyond the independent-particle approximation, are needed in order to fully account for the experimental trend. Evidentially, more detailed experimental and theoretical investigations are required to solve this ongoing uncertainty over the precise origin of absorption and emission in these double perovskite compounds.

Since we expected these double perovskites to have a weakly absorbing indirect band gap and potentially also have a high density of sub band gap defect states, we performed photothermal deflection optical absorption spectroscopy (PDS) on our thin films (Fig. S11 in the SI) to investigate the region below the band-gap. The PDS spectrum curves clearly show panchromatic absorption below the bandgap, indicating the presence of sub-bandgap states. The Urbach energy, which represents the electronic disorder at the band edge, was calculated through a fitting on the PDS data (Figure S12). With the values reported in Table ST6 we can observe that the Urbach

energy ranges from 50 to 65 meV, which are larger than those determined for lead and tin halide perovskites [36-38]. This difference in E_u is consistent with the lower performances of all-inorganic perovskites, especially in terms of V_{oc} [39]. Table ST4 reports the bandgap extrapolated from a Tauc-plot analysis and indicates a clear enlargement with increasing indium percentage, going from 2.19 eV for TF0 to 2.33 eV for TF60.

Finally, to assess if the indium alloying can have a positive effect upon optoelectronic devices, we prepared planar heterojunction photovoltaic devices in the *n-i-p* architecture, employing SnO_2 nanoparticles as the n-type charge extraction layer and doped spiro-OMeTAD as the p-type charge extraction layer. Full details of device fabrication and testing are given in the SI.

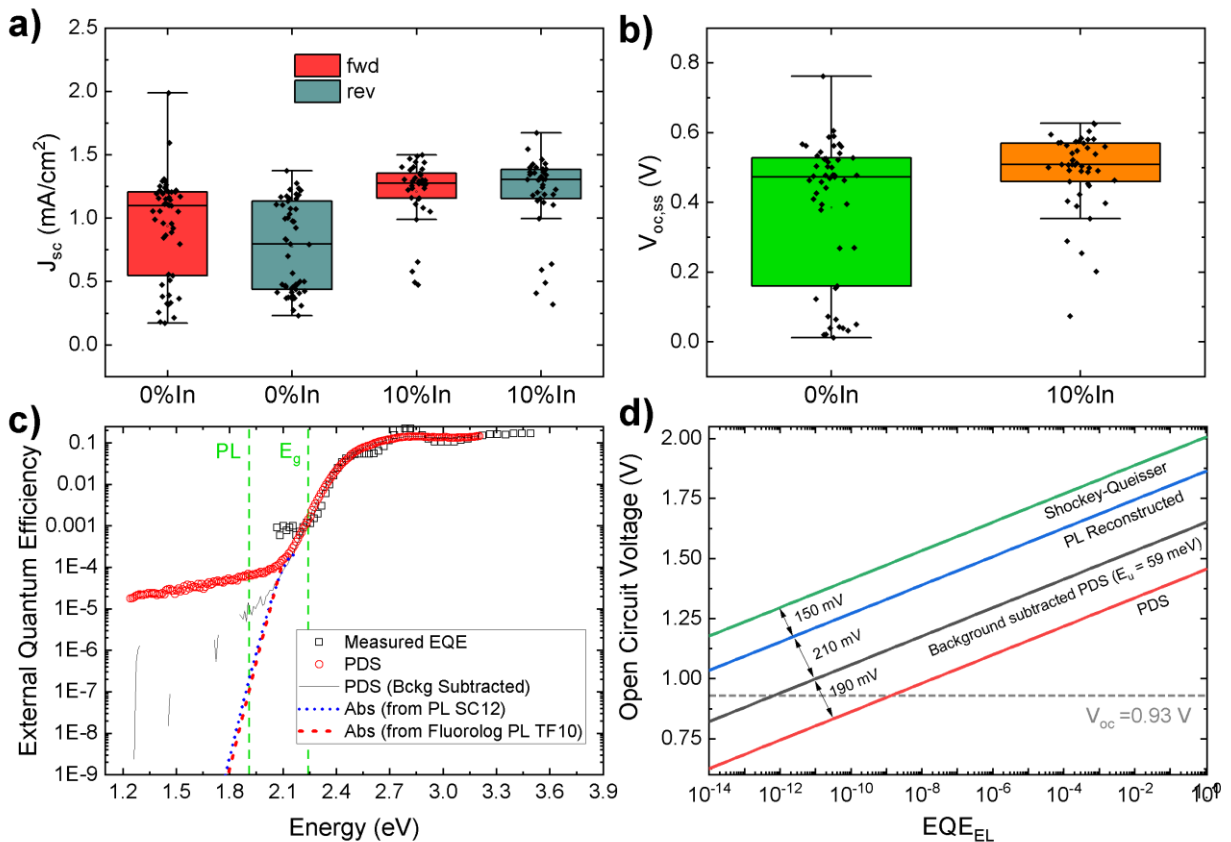


Figure 4 a) short-circuit current and b) Steady-state open-circuit voltage (box plot) for $\text{Cs}_2\text{AgBiBr}_6$ and the 10% indium-alloyed compound. c) The black squares represent the measured External Quantum

Efficiency, the red circles and black line the measured PDS without and with a linear background subtraction respectively, and the blue and red dashed line the reconstructed absorption from the PL measured on SC12 and TF10 respectively. d) Open circuit voltage calculated using detailed balance for spectra shown in panel c). The dashed line in this panel indicates the highest open-circuit voltage measured on our devices (see Fig S15b).

As previously reported, these double-perovskites present strong hysteresis between the forward (from V_{OC} to J_{SC}) and the reverse (from J_{SC} to V_{OC}) scan, as we can notice from the JV curves in Figure S15 in the SI. In addition, the performances of these devices are poorly reproducible, varying from batch to batch. For this reason we deem it more indicative and useful to observe the averaged current-density-voltage curve performances parameters, rather than the single JV scans. In Figure 4a and 4b we show the short-circuit current densities and the open-circuit voltage for a single batch of cells comparing the neat bismuth to the 10% indium alloyed double perovskite, measured under AM1.5 simulated sunlight. We can observe from panel 4a that the addition of 10% indium improves the short-circuit current in both the reverse and forward scans, and this results in an overall improvement of the PCE shown in the SI. Panel 4b shows the steady-state open-circuit voltage (V_{SS}), we can notice that the spread in data decreases in the measurement of devices with indium, and the steady-state open-circuit voltage is slightly higher.

For a bandgap of 2.23 eV, the Shockley-Queisser formalism [40,41] predicts a limiting PCE of 18% with $V_{OC} = 1.91$ V, $J_{SC} = 10.14$ mA/cm² and FF = 0.93. However, the best Cs₂AgBiBr₆ based cells today only reach 2.8% PCE ($V_{OC} = 1.06$ V, $J_{SC} = 5.13$ mA/cm², FF=0.52) [42]. Longo et al. have shown that the large current deficit is due to poor electron diffusion length (tens of nm) [43]. This is likely to be true for the indium alloyed material as well. The difference between the band gap energy and the open-circuit voltage a cell can generate is a good measure of the minimum energy loss in the photovoltaic cell, which is often referred to as a voltage deficit or loss-in-

potential. For a material with a band gap of 2.23 eV, the minimum voltage deficit for an ideal cell is 320 mV. However, our best experimental cell shows a maximum V_{OC} of only 0.93V (Figure S15b in the SI) and hence a voltage deficit of over 1400 mV. To understand this result we need to assess what causes this voltage deficit, if it is a fundamental barrier for this material ever being efficient, or if there are potential solutions to overcoming a large fraction of these deficiencies.

The voltage deficit may originate from a combination of factors, including high dark recombination current densities (due to the fundamental optical properties of the material), a significant fraction of non-radiative recombination (resulting from high defect densities in the bulk of the absorber material), high surface recombination velocities on the surface of the absorber layer, and high surface recombination at the absorber layer / charge extraction layer interfaces. Furthermore, poor charge carrier selectivity of the transport layers may also inhibit open-circuit voltage [44,45].

From a fundamental standpoint, even in the absence of defects and interfaces responsible for non-radiative recombination, the sub band gap optical properties of a solar absorber layer can strongly influence the maximum open-circuit voltage a material can achieve when integrated into a solar cell. This is because the dark-recombination current density (J_0) can be calculated by taking the overlap integral of the black body radiation at the background temperature ($T \sim 300K$), with the external quantum efficiency spectra of the solar cell. Since the black body radiation spectra at ambient temperature increases exponentially towards lower energies, the overall J_0 is most strongly influenced by absorption properties in the sub band gap region of the absorber layer. In the first instance, this can be quantified by the steepness of the absorption onset just below the band gaps, as the aforementioned Urbach energy. If the Urbach energy is less than the thermal energy at the operation temperature ($k_B T \sim 25$ meV at 300K, where k_B is the Boltzmann constant), then the

additional voltage deficit, beyond that calculated via the Shockley-Queisser (SQ) treatment (which assumes a step function absorption onset), is close to negligible (few tens of meV). However, once the Urbach energy increases beyond $k_B T$, then the voltage-deficit becomes increasingly significant [39].

We quantified this loss for our $\text{Cs}_2\text{AgBi}_{0.9}\text{In}_{0.1}\text{Br}_6$ material using the principle of detailed balance. This calculation takes the absorber's absorptance as input and then predicts the V_{OC} assuming that all the recombination is radiative, i.e. in the radiative limit [46,47]. This in principle provides a lower-bound for the V_{OC} loss, which would be the voltage expected if all other non-radiative recombination paths were eliminated. We performed this calculation under different assumptions to illustrate a range of possibilities, since the properties of this material are not yet entirely understood. Using the measured PDS absorption as input for the detailed balance calculation, we estimate the voltage deficit in the radiative limit to be at least 870 mV, which is 550 mV greater than the S-Q limit V_{oc} . We note that if the tail extends below 1.3 eV (the limit of our detector), the loss is expected to be even more. However, we also consider the possibility that the PDS absorption plateau below 2.1 eV is due to free carrier absorption, or sub-band gap defects which are not part of the continuum of states, and not a fundamental property of the material [48]. When we subtract this panchromatic sub band gap absorption feature (see SI), the resulting ~ 59 meV Urbach tail results in a V_{OC} deficit of 680 mV from band gap, and 360 mV greater loss than in the SQ limit. The mechanism of PL emission in this material is yet unknown. In the case that it is band-to-band recombination, the radiative states can be reconstructed, often to extremely low values, using emission-absorption reciprocity [49,50]. We follow the reciprocity approach and use these reconstructed states to extend our measured absorption spectra down to lower energies (Fig

4c). Using this “PL reconstructed absorption spectra” we estimate the V_{OC} deficit to be 470 mV from the band gap, which is only 150 mV greater than the SQ limit.

By definition, the external radiative efficiency (ERE) is below 1. To put this into context, the highest performing Si, GaAs, CdTe and lead-halide perovskite cells have ERE’s of ~ 0.01 , 0.3, 0.00008, and 0.06 respectively [51,52]. In Fig. 4d, we show the open-circuit voltage for our $Cs_2AgBi_{0.9}In_{0.1}Br_6$ cell, which we calculate following the detailed balance principle, as a function of ERE. As it is clearly apparent, the fundamental offset from the SQ voltage, related to shallow absorption onset and sub band gap absorptions, remains constant across all values of ERE. As inferred by comparing our achieved open-circuit voltage to the calculated values, the maximum ERE of our cell will range from 10^{-10} to 10^{-15} , depending upon what is the truest reflection of the absorption edge in this material. This indicates that the primary target for immediate improvement in the $Cs_2AgBi_{0.9}In_{0.1}Br_6$ PV cells is to focus upon enhancing ERE.

In conclusion, we have shown that the presence of indium in the $Cs_2AgBi_{1-x}In_xBr_6$ structure contracts the unit cells and makes the cubic phase more stable, resulting in a reduction of the cubic to tetragonal phase transition temperature. Concerning optoelectronic properties, we found that a small percentage of indium enhances the photoluminescence intensity and improves the photovoltaic performances of devices, showing almost doubled J_{sc} and PCE when 10% indium is added in the structure. However, these devices remain considerably less efficient than lead halide perovskite PV cells, leading us to assess the losses in the material from a fundamental perspective. We determine that significant losses in open-circuit voltage are present due to a shallow onset of the absorption edge, combined with significant sub-band gap absorption. However, if improvements can be made to the material to “clean up” the panchromatic sub-band gap absorptions, additional losses beyond that of the SQ limit of only 150 mV would be achievable.

At present, the majority of the losses originate from low radiative efficiency. This indicates that fundamentally, this material may prove to be useful as a solar absorber material where a wide band gap absorber is required. However, immediate attention is required to understand and mitigate the role and presence of non-radiative defect sites in the absorber material, and the nature of non-radiative recombination and non-selectivity at the charge extraction layer/absorber layer heterojunctions. Concerning the absorber material itself, the band gap is non-ideal for use in PV cells, being too wide at 2.35 eV for optimum use as a top cell in both tandem ($E_g \sim 1.65$ eV required) and even triple junction cells ($E_g \sim 2.05$ eV required) [53]. Therefore strategies to reduce the band gap are likely to lead to improved performance and utility. These should probably focus upon strategies to stabilize iodide in the $\text{Cs}_2\text{AgBiX}_6$ framework, or by exploring the broader Ag-Bi halide materials space [54]. It is probable that indium substitution will be broadly applicable for enhancing the luminescence of these material families. For light emission applications, green and red emission would be favorable for the use of these compounds as phosphors. For that purpose, chlorine doping is likely to prove useful.

Supporting information

The Supporting Information is available free of charge on the ACS Publications website at DOI: XXXX

Indium percentage determined by ICP-MS and XRD in single crystals (TS1) and powders (TS4); Plot of F^2_{calc} versus F^2_{obs} for the structural refinement of $\text{Cs}_2\text{AgIn}_x\text{Bi}_{1-x}\text{Br}_6$ single crystals (Fig. S1) and structural information (Table ST2); Rietveld refinements for $\text{Cs}_2\text{AgIn}_x\text{Bi}_{1-x}\text{Br}_6$ powders (Fig. S2) and related structural information (Table ST3). Thin film thickness (Table ST5); thin-films XRD patterns (Fig. S3). Structural transitions in single crystals (Fig. S4, S5, and S6). Absorption and PL from polycrystalline powders (Fig. S7), photos of samples (Fig. S8). Optical constants n and k

from ellipsometry measurements (Fig. S9). Computational methods (Section 4). PDS and Tauc-plot (Fig. S11); band gaps and Urbach energies extrapolated from fittings (Table ST6 and Fig. S12). Device preparation and characterization in Section 6: J-V curves (Fig. S13), EQE (Fig. S14), PCE and V_{OC} (Fig. S15).

Notes

The authors declare no competing financial interest.

ACKNOWLEDGMENT

This work was part funded by the Engineering and Physical Sciences Research Council (EPSRC) UK, under EP/S004947/1. L.S. acknowledges financial support from the UK Engineering and Physical Sciences Research Council (EPSRC) and from Balliol college at Oxford University (J.T. Hamilton scholarship). G.V. acknowledges funding from the Chaire de Recherche Rennes Metropole project. F.G. was supported by the Robert A. Welch Foundation under award number F-1990-20190330. M.A.-J. thanks Cambridge Materials Limited, Wolfson College, University of Cambridge, and the Royal Society for their funding and technical support. S.V.K. expresses gratitude to EPSRC (WAFT, Grant No. EP/M015173/1) for the spectroscopic ellipsometer. S.M. gratefully acknowledges funding from the Rhodes Scholarships.

REFERENCES

- (1) NREL efficiency chart <https://www.nrel.gov/pv/cell-efficiency.html> (accessed on: 6

August 2020)

- (2) Lee, M. M.; Teuscher, J.; Miyasaka, T.; Murakami, T. N. and Snaith, H. J. Efficient Hybrid Solar Cells Based on Meso-Superstructured Organometal Halide Perovskites. *Science* **2012**, 338(6107), 643-647.
- (3) Kojima, A.; Teshima, K.; Shirai, Y. and Miyasaka, T. Organometal Halide Perovskites as Visible-Light Sensitizers for Photovoltaic Cells. *J. Am. Chem. Soc.* **2009**, 131, 17, 6050–6051.
- (4) Kim, H. S.; Lee, C. R.; Im, J. H.; Lee, K. B.; Moehl, T.; Marchioro, A.; Moon, S. J.; Humphry-Baker, R.; Yum, J. H.; Moser, J. E.; Grätzel, M. and Park, N. G. Lead Iodide Perovskite Sensitized All-Solid-State Submicron Thin Film Mesoscopic Solar Cell with Efficiency Exceeding 9%. *Sci. Rep.* **2012** 2, 591.
- (5) Bi, D.; Tress, W.; Dar, M. I.; Gao, P.; Luo, J.; Renevier, C.; Schenk, K.; Abate, A.; Giordano, F.; Baena, J.-P. C. et al. Efficient Luminescent Solar Cells Based on Tailored Mixed-Cation Perovskites. *Sci. Adv.* **2016**, 2, e1501170.
- (6) Snaith, H. J. Perovskites: The Emergence of a New Era for Low Cost, High-Efficiency Solar Cells. *J. Phys. Chem. Lett.* **2013**, 4, 3623-3630.
- (7) Lee, M. M.; Teuscher, J.; Miyasaka, T.; Murakami, T. N.; Snaith, H. J. Efficient Hybrid Solar Cells Based on Meso-Superstructured Organometal Halide Perovskites. *Science* **2012**, 338, 643-647.
- (8) Koh, T. M.; Fu, K.; Fang, Y.; Chen, S.; Sum, T. C.; Mathews, N.; Mhaisalkar, S. G.; Boix, P. P.; Baikie, T. Formamidinium-Containing Metal-Halide: An Alternative

- Material for Near-IR Absorption Perovskite Solar Cells. *J. Phys. Chem. C* **2014**, 118, 16458-16462.
- (9) Lee, J.-W.; Seol, D.-J.; Cho, A.-N.; Park, N.-G. High-Efficiency Perovskite Solar Cells Based on the Black Polymorph of HC-(NH₂)₂PbI₃. *Adv. Mater.* **2014**, 26, 4991-4998.
- (10) Deretzis, I.; Alberti, A.; Pellegrino, G.; Smecca, E.; Giannazzo, F.; Sakai, N.; Miyasaka, T. and La Magna, A. Atomistic Origins of CH₃NH₃PbI₃ Degradation to PbI₂ in Vacuum. *Appl. Phys. Lett.* **2015**, 106, 131904.
- (11) Dualeh, A.; Gao, P.; Seok, S. I.; Nazeeruddin, M. K. and Grätzel, M. Thermal Behavior of Methylammonium Lead-Trihalide Perovskite Photovoltaic Light Harvesters. *Chem. Mater.* **2014**, 26, 6160-6164.
- (12) Han, Y.; Meyer, S.; Dkhissi, Y.; Weber, K.; Pringle, J. M.; Bach, U.; Spiccia, L. and Cheng, Y.-B. Degradation Observations of Encapsulated Planar CH₃NH₃PbI₃ Perovskite Solar Cells at High Temperatures and Humidity. *J. Mater. Chem. A* **2015**, 3, 8139-8147.
- (13) Tan, K. W.; Moore, D. T.; Saliba, M.; Sai, H.; Estroff, L. A.; Hanrath, T.; Snaith, H. J. and Wiesner, U. Thermally Induced Structural Evolution and Performance of Mesoporous Block Copolymer-Directed Alumina Perovskite Solar Cells. *ACS Nano* **2014**, 8, 4730-4739.
- (14) Sutton, R. J.; Eperon, G. E.; Miranda, L.; Parrott, E. S.; Kamino, B. A.; Patel, J. B.; Hörantner, M. T.; Johnston, M. B.; Haghighirad, A. A.; Moore, D. T. and Snaith, H. J. Bandgap-Tunable Cesium Lead Halide Perovskites with High Thermal Stability for Efficient Solar Cells. *Adv. Energy Mater.* **2016**, 6, 1502458.

- (15) Wang, Y.; Zhang, T.; Xu, F.; Li, Y.; and Zhao, Y. A Facile Low Temperature Fabrication of High Performance CsPbI₂Br All-Inorganic Perovskite Solar Cells *Sol. RRL* **2018**, 2, 1700180.
- (16) Li, Z. and Yin, W. Recent Progress in Pb-Free Stable Inorganic Double Halide Perovskites. *J. Semicond.* **2018**, 39, 071003.
- (17) Giustino, F. and Snaith, H. J. Toward Lead-Free Perovskite Solar Cells. *ACS Energy Lett.* **2016**, 1, 6, 1233–1240.
- (18) Wu, C.; Zhang, Q.; Liu, Y.; Luo, W.; Guo, X.; Huang, Z.; Ting, H.; Sun, W.; Zhong, X.; Wei, S. et al. The Dawn of Lead-Free Perovskite Solar Cell: Highly Stable Double Perovskite Cs₂AgBiBr₆ Film. *Adv. Sci. (Weinheim, Ger.)* **2018**, 5, 1700759.
- (19) Volonakis, G.; Filip, M. R.; Haghighirad, A. A.; Sakai, N.; Wenger, B.; Snaith, H. J.; Giustino, F. Lead-Free Halide Double Perovskites via Heterovalent Substitution of Noble Metals. *J. Phys. Chem. Lett.* **2016**, 7, 1254-1259.
- (20) Slavney, A. H.; Hu, T.; Lindenberg, A. M.; Karunadasa, H. I. A Bismuth-Halide Double Perovskite with Long Carrier Recombination Lifetime for Photovoltaic Applications. *J. Am. Chem. Soc.* **2016**, 138, 2138-2141.
- (21) Zelewski, S. J.; Urban, J. M.; Surrente, A.; Maude, D. K.; Kuc, A.; Schade, L.; Johnson, R. D.; Dollmann, M.; Nayak, P. K.; Snaith, H. J.; Radaelli, P.; Kudrawiec, R.; Nicholas, R. J.; Plochocka, P. and M. Baranowski. Revealing the Nature of Photoluminescence Emission in Metal-Halide Double Perovskite Cs₂AgBiBr₆. *J. Mat. Chem. C* **2019**, 7(27), 8350–8356.

- (22) Gao, W.; Ran, C.; Xi, J.; Jiao, B.; Zhang, W.; Wu, M.; Hou, X.; Wu, Z.; High-Quality Cs₂AgBiBr₆ Double Perovskite Film for Lead Free Inverted Planar Heterojunction Solar Cells with 2.2% Efficiency. *ChemPhysChem* **2018**, 19, 1696.
- (23) Shang, M.-H.; Zhang, J.; Zhang, P.; Yang, Z.; Zheng, J.; Haque, M. A.; Yang, W.; Wei, S.-H. and Wu, T. Stable Bandgap-tunable Hybrid Perovskites with Alloyed Pb-Ba Cations for High-Performance Photovoltaic Applications. *J. Phys. Chem. Lett.* **2019**, 10, 1, 59-66.
- (24) Du, K. Z.; Meng, W.; Wang, X.; Yan, Y. and Mitzi, D. B. Bandgap Engineering of Lead-Free Double Perovskite Cs₂AgBiBr₆ Through Trivalent Metal Alloying. *Angew. Chem. Int.* **2017**, 56, 8158-8162.
- (25) Luo, J.; Wang, X.; Li, S.; Liu, J.; Guo, Y.; Niu, G.; Yao, L.; Gao, L.; Dong, Q.; Zhao, C. *et al.* Efficient and Stable Emission of Warm-White Light from Lead-Free Halide Double Perovskites. *Nature* **2018**, 563, 541-545.
- (26) Schade, L.; Wright, A. D.; Johnson, R. D.; Dollmann, M.; Wenger, B.; Nayak, P. K.; Prabhakaran, D.; Herz, L. M.; Nicholar, R.; Snaith, H. J. and Radaelli, P. G. Structural and Optical Properties of Cs₂AgBiBr₆ Double Perovskite. *ACS Energy Lett.* **2019**, 4, 1, 299-305.
- (27) Wruck, B. Einfluß des Na-Gehaltes und der Al, Si-Fehlordnung auf das thermodynamische Verhalten der Phasenumwandlung P1-15 in Anorthit. *Dissertation Univ Hannover* **1986**
- (28) Schmitz, A.; Schaberg, L. L.; Sirotinskaya, S.; Pantaler, M.; Lupascu, D. C.; Benson, N. and Bacher, G. Fine Structure of the Optical Absorption Resonance in Cs₂AgBiBr₆ Double Perovskite Thin Films. *ACS Energy Lett.* **2020**, 5, 559-565.

- (29) Kentsch, R.; Scholz, M.; Horn, J.; Schlettwein, D.; Oum, K.; Lenzer, T. Exciton Dynamics and Electron–Phonon Coupling Affect the Photovoltaic Performance of the Cs₂AgBiBr₆ Double Perovskite. *J. Phys. Chem. C* **2018**, 122 (45), 25940–25947.
- (30) Yang, B.; Chen, J.; Yang, S.; Hong, F.; Sun, L.; Han, P.; Pullerits, T.; Deng, W.; Han, K. Lead-Free Silver-Bismuth Halide Double Perovskite Nanocrystals. *Angew. Chem., Int. Ed.* **2018**, 57 (19), 5359–5363.
- (31) Connor, B. A.; Leppert, L.; Smith, M. D.; Neaton, J. B.; Karunadasa, H. I. Layered Halide Double Perovskites: Dimensional Reduction of Cs₂AgBiBr₆. *J. Am. Chem. Soc.* **2018**, 140 (15), 5235– 5240.
- (32) Bekenstein, Y.; Dahl, J. C.; Huang, J.; Osowiecki, W. T.; Swabeck, J. K.; Chan, E. M.; Yang, P.; Alivisatos, A. P. The Making and Breaking of Lead-Free Double Perovskite Nanocrystals of Cesium Silver-Bismuth Halide Compositions. *Nano Lett.* **2018**, 18 (6), 3502– 3508.
- (33) Zacharias, M. and Giustino, F. Theory of the Special Displacement Method for Electronic Structure Calculations at Finite Temperature. *Phys. Rev. Research* **2020** 2, 013357.
- (34) Popescu, V. and Zunger, A. Extracting E Versus k Effective Band Structure from Supercell Calculations on Alloys and Impurities *Phys. Rev. B* **2012** 85, 085201.
- (35) Volonakis, G.; Haghghirad, A. A.; Milot, R. L.; Sio, W. H. S.; Filip, M. R.; Wenger, B.; Johnston, M. B.; Herz, L. M.; Snaith, H. J. and Giustino, F. Cs₂InAgCl₆: A New Lead-Free Halide Double Perovskite with Direct Band Gap. *J. Phys. Chem. Lett.* **2017**, 8, 4, 772-778.

- (36) De Wolf, S.; Holovsky, J.; Moon, S.-J.; Löper, P.; Niesen, B.; Ledinsky, M.; Haug, F.-J.; Haug, F.-J.; Yum, J.-H.; Ballif, C. Organometallic Halide Perovskites: Sharp Optical Absorption Edge and Its Relation to Photovoltaic Performance. *J. Phys. Chem. Lett.* **2014**, *5*, 1035.
- (37) Luo, D.; Yang, W.; Wang, Z.; Sadhanala, A.; Hu, Q.; Su, R.; Shivanna, G. F.; Trindade, J. F.; Watts, Z.; Xu, T. *et al.* Enhanced Photovoltage for Inverted Planar Heterojunction Perovskite Solar Cells. *Science* **2018**, *360*, 1442.
- (38) Abdi-Jalebi, M.; Dar, M. I.; Sadhanala, A.; Senanayak, S. P.; Franckevičius, M.; Hu, Y.; Nazeeruddin, M. K.; Zakeeruddin, S. M.; Grätzel, M. *et al.* Impact of Monovalent Cation Halide Additives on the Structural and Optoelectronic Properties of CH₃NH₃PbI₃ Perovskite. *Adv. Energy Mater.* **2016**, *6*, 1502472.
- (39) Nayak, P. K.; Mahesh, S.; Snaith, H. J. and Cahen, D. Photovoltaic Solar Cell Technologies: Analysing the State of the Art. *Nat. Rev. Mat.* **2019**, *4*, 269-285.
- (40) Shockley, W. & Queisser, H. J. Detailed Balance Limit of Efficiency of p-n Junction Solar Cells. *J. Appl. Phys.* 1961, *32*, 510–519.
- (41) Guillemoles, J. F., Kirchartz, T., Cahen, D. & Rau, U. Guide for the Perplexed to the Shockley–Queisser Model for Solar Cells. *Nature Photonics* **2019** *13*, 501–505.
- (42) Yang, X.; Chen, Y.; Liu, P.; Xiang, H.; Wang, W.; Ran, R.; Zhou, W. and Shao, Z. Simultaneous Power Conversion Efficiency and Stability Enhancement of Cs₂AgBiBr₆ Lead-Free Inorganic Perovskite Solar Cell through Adopting a Multifunctional Dye Interlayer. *Adv. Funct. Mater.* **2020** *30*, 2001557.
- (43) Longo, G.; Mahesh, S.; Buizza, L. R. V.; Wright, A. D.; Ramadan, A. J.; Abdi-Jalebi, M.; Nayak, P. K.; Herz, L. M. and Snaith, H. J. Understanding the Performance-

- Limiting Factors of Cs₂AgBiBr₆ Double-Perovskite Solar Cells. *ACS Energy Lett.* **2020** 5, 7, 2200–2207.
- (44) Onno, A.; Chen, C. and Holman, Z. C. Electron and Hole Partial Specific Resistances: a Framework to Understand Contacts to Solar Cells. *IEEE 46th Photovoltaic Specialists Conference (PVSC) Chicago, IL, USA* **2019** 2329-2333.
- (45) Le Corre, V. M.; Stolterfoht, M.; Toro, L. P.; Feuerstein, M.; Wolff, C.; Gil-Escrig, L.; Bolink, H. J.; Neher, S. and Koster, J. A. Charge Transport Layers Limiting the Efficiency of Perovskite Solar Cells: How to Optimize Conductivity, Doping, and Thickness. *ACS Appl. Energy Mater.* **2019** 2, 9, 6280-6287.
- (46) Mahesh, S. *et al.* Revealing the Origin of Voltage Loss in Mixed-Halide Perovskite Solar Cells. *Energy Environ. Sci.* **2019** 50, 675.
- (47) Rau, U. Reciprocity Relation Between Photovoltaic Quantum Efficiency and Electroluminescent Emission of Solar Cells. *Phys. Rev. B - Condens. Matter Mater. Phys.* **2007** 76, 1–8.
- (48) Zhao, B.; Abdi-Jalebi, M.; Tabachnyk, M.; Glass, H.; Kamboj, V. S.; Nie, W.; Pearson, A. J.; Puttison, Y.; Gödel, K. C.; Beere, H. E. *et al.* High Open-Circuit Voltages in Tin-Rich Low-Bandgap Perovskite-Based Planar Heterojunction Photovoltaics. *Adv. Mat.* **2016** 29, 2.
- (49) Wurfel, P. The Chemical Potential of Radiation. *J. Phys. C Solid State Phys.* **1982** 15, 3967–3985.
- (50) Daub, E. & Würfel, P. Ultralow Values of the Absorption Coefficient of Si Obtained from Luminescence. *Phys. Rev. Lett.* **1995** 74, 1020–1023.
- (51) Green, M. A and Ho-Baillie, A. W. Y. Pushing the Limit: Radiative Efficiencies of

- Recent Mainstream and Emerging Solar Cells. *ACS Energy Letters* **2019** 4, 7, 1639-1644.
- (52) deQuilettes, D. W.; Laitz, M.; Brenes, R.; Dou, B.; Motes, B. T.; Stranks, S. D.; Snaith, H. J.; Bulović, V. and Ginger, D. S. Maximizing the External Radiative Efficiency of Hybrid Perovskite Solar Cells. *Pure Appl. Chem.* **2020** 92, 5, 697-706.
- (53) Höranter, M. T.; Leijtens, T.; Ziffer, M. E.; Eperon, G. E.; Christoforo, M. G.; McGehee, M. D. and Snaith, H. J. The Potential of Multijunction Perovskite Solar Cells. *ACS Energy Lett.* **2017**, 2, 10, 2506-2513.
- (54) Jin, Z.; Zhang, Z.; Xiu, J.; Song, H.; Gatti, T. and He, Z. A Critical Review on Bismuth and Antimony Halide Based Perovskites and Their Derivatives for Photovoltaic Applications: Recent Advances and Challenges. *J. Mater. Chem. A* **2020**, 8, 16166-16188.
-